PCCP

PAPER

View Article Online
View Journal | View Issue

Cite this: *Phys. Chem. Chem. Phys.*, 2022, **24**, 16101

Infrared spectra and structures of protonated amantadine isomers: detection of ammonium and open-cage iminium ions†

Martin Andreas Robert George and Otto Dopfer *

The protonated form of amantadine (1-$C_{10}H_{15}NH_2$, Ama), the amino derivative of adamantane ($C_{10}H_{16}$, Ada), is a wide-spread antiviral and anti-Parkinsonian drug and plays a key role in many pharmaceutical processes. Recent studies reveal that the adamantyl cage ($C_{10}H_{15}$) of Ama can open upon ionization leading to distonic bicyclic iminium isomers, in addition to the canonical nascent Ama^+ isomer. Herein, we study protonation of Ama using infrared photodissociation spectroscopy (IRPD) of Ar-tagged ions and density functional theory calculations to characterize cage and open-cage isomers of $AmaH^+$ and the influence of the electron-donating NH_2 group on the cage-opening reaction potential. In addition to the canonical ammonium isomer ($AmaH^+$(**I**)) with an intact adamantyl cage, we identify at least one slightly less stable protonated bicyclic iminium ion ($AmaH^+$(**II**)). While the ammonium ion is generated by protonation of the basic NH_2 group, $AmaH^+$(**II**) is formally formed by H addition to a distonic bicyclic iminium ion produced upon ionization of Ama and subsequent cage opening.

Received 28th April 2022,
Accepted 12th June 2022

DOI: 10.1039/d2cp01947g

rsc.li/pccp

Introduction

Amantadine (Ama, 1-tricyclo[3.3.1.1^{3,7}]decylamine, 1-adamantylamine, 1-aminoadamantane, $C_{16}H_{15}NH_2$) is the amino derivative of adamantane ($C_{10}H_{16}$, Ada), the parent molecule of the group of diamondoids.[1] These nm-sized H-passivated nanodiamonds are rigid, stress-free, and highly stable cycloalkanes and form a fundamental class of saturated sp^3-hybridized hydrocarbon molecules,[2–4] with (potential) applications in a wide range of disciplines including materials science, molecular electronics, medical sciences, chemical synthesis, and astrochemistry.[5–17] For example, radical cations of diamondoids are predicted to be intermediates in substitution reactions in polar solvents.[14,18–21] Based on the detection of several amines[22] and protonated molecules[22–24] in the interstellar medium and the likely presence of diamondoids,[22] the occurrence of Ama and its protonated form is also expected.[13,25,26]

Amantadine, particularly in its N-protonated form, belongs to the most important diamondoid derivatives, because of its use in pharmaceutical applications as antiviral and anti-Parkinsonian drug. It is successfully marketed under several brand names, including Symmetrel® (Ama·HCl), Gocovri®, Symadine®, and Osmolex ER®.[15,27–30] In all postulated mechanisms, N-protonated Ama (or its dimethylated derivative memantine, Namenda®) is the biochemically active species.[31,32] Ama is effective in the prophylaxis and treatment of influenza A infections by preventing the virus from entering the host cell through blocking of the ion channel.[33–35] However, due to drug resistance, its use is no longer recommended for influenza.[36,37] Although the mechanism of action against Parkinsonism is not yet fully understood, the drug enhances the release of dopamine from nerve endings of brain cells, along with stimulating the norepinephrine response.[38–40] In addition to its pharmaceutical use, Ama has antagonistic effects on NMDA (*N*-methyl-D-aspartate) receptors[41,42] and is discussed for treating other diseases such as multiple sclerosis, depression, and cocaine addiction.[43–45] In 2013, memantine was in the top 100 best-selling drugs worldwide, with sales exceeding $10^9.[46]

In addition to its pharmaceutical use, the diamondoid derivative Ama is also of interest for studying ionization-induced rearrangement processes of the adamantyl cage.[47,48] By replacing H with the electron-donating NH_2 group at the apical 1-position,[42,49] the chemical properties of diamond-like structures are mostly retained but the barrier to cage opening is strongly reduced.[47,48] The geometric, vibrational, and electronic properties of Ama are well-known from infrared (IR), Raman, and electron momentum spectroscopy.[50–54] Low-resolution electron momentum spectra show that ionization of Ama to the electronic ground state of the cation occurs by electron ejection from the nonbonding N lone pair of the NH_2 group (HOMO), with a rough estimate of the vertical ionization

Institut für Optik und Atomare Physik, Technische Universität Berlin, Hardenbergstr. 36, 10623 Berlin, Germany. E-mail: dopfer@physik.tu-berlin.de

† Electronic supplementary information (ESI) available. See DOI: https://doi.org/10.1039/d2cp01947g

energy of 8.6 eV.[53] In our recent IR spectroscopic and quantum chemical studies of Ama^+L_n clusters (with L = Ar, N_2, H_2O),[47,48,55] we identified, in addition to the canonical nascent Ama^+(**I**) isomer with an intact $C_{10}H_{15}$ cage, two distonic bicyclic iminium isomers Ama^+(**II**) and Ama^+(**III**) in which the adamantyl cage opens upon ionization. H → NH_2 substitution drastically lowers all barriers for the rearrangement processes, because of the strongly p/π-electron donating character of the NH_2 group, which leads to high and thus detectable yields for the formation of Ama^+(**II**) and Ama^+(**III**). Starting from the cage structure Ama^+(**I**) produced by vertical ionization of Ama (E_0 = 46 kJ mol^{-1}), C–C bond activation opens the adamantyl cage forming the primary radical Ama^+(**II**) (E_0 = 87 kJ mol^{-1}) *via* a boat → chair conversion of one of the cyclohexane rings. In a subsequent 1,2 H-shift accompanied by chair → boat back conversion, the much more stable tertiary radical Ama^+(**III**) is generated (E_0 = 0 kJ mol^{-1}). Interestingly, no open-cage isomers were detected in previous IR and optical spectra of Ada^+ and its clusters generated in the same type of ion source due to ionization from a different orbital and higher reaction barriers.[26,56,57] Instead of ionization of Ama, we characterize herein the effects of protonation using the same IR spectroscopic and quantum chemical tools to determine the structure of protonated amantadine, the impact of the electron-withdrawing NH_3^+ group on the adamantyl cage of $AmaH^+$, and the possible formation of open-cage isomers. Experimentally, we apply IR photodissociation (IRPD) spectroscopy to mass-selected Ar-tagged $AmaH^+$ ions, whereby the weakly-bonded Ar ligand has essentially no impact on the structural, energetic, vibrational, and chemical properties of $AmaH^+$, as recently demonstrated for the Ama^+ radical cation.[47,48] Despite its high pharmaceutical importance, no spectroscopic studies are available for isolated $AmaH^+$. Mass spectrometry experiments provide information about its fragmentation and proton affinity.[58] Several spectrophotometric, NMR and IR studies of the amantadine hydrochloride salt (Ama·HCl) focus mostly on analytical applications of this drug molecule.[54,59–62]

2. Experimental and computational techniques

IRPD spectra of $AmaH^+Ar$ are recorded in a quadrupole–octupole–quadrupole tandem mass spectrometer coupled to an electron ionization source described elsewhere.[63,64] The clusters are produced in a pulsed supersonic plasma expansion by electron and/or chemical ionization (EI/CI) close to the nozzle orifice followed by clustering reactions. The expanding gas mixture is generated by passing a carrier gas mixture of 5% H_2/He and Ar in the ratio of 1 : 50 through a heated reservoir containing Ama (Sigma Aldrich, >97%, $T \sim 130^\circ$) at a stagnation pressure of 5–9 bar. The filaments of the EI source are operated with an offset voltage of 220 V, which determines the upper limit for the kinetic energy of the electrons hitting the molecules in the expansion. A typical mass spectrum of the ion source is shown in the electronic supporting information (Fig. S1, ESI†). One possible production route for $AmaH^+Ar$ involves EI of H_2 (eqn (1)) followed by exothermic proton transfer reactions (eqn (2) and (3)) to generate $AmaH^+$ and three-body collisions to form the $AmaH^+Ar$ clusters (eqn (4)):[65,66]

$$H_2 + e \rightarrow H_2^+ + 2e \quad (1)$$

$$H_2^+ + H_2 \rightarrow H_3^+ + H \quad (2)$$

$$Ama + H_3^+ \rightarrow AmaH^+ + H_2 \quad (3)$$

$$AmaH^+ + Ar + M \rightarrow AmaH^+Ar + M \quad (4)$$

Reaction (3) is highly exothermic (by 557 kJ mol^{-1} at the B3LYP-D3/cc-pVTZ level) and thus may lead to opening of the adamantyl cage. An alternative route for the formation of $AmaH^+$ involves EI/CI of Ama to form the Ama^+ radical cation (eqn (5)), which then reacts with H_2 to generate $AmaH^+$ (eqn (6)):

$$Ama + e \rightarrow Ama^+ + 2e \quad (5)$$

$$Ama^+ + H_2 \rightarrow AmaH^+ + H \quad (6)$$

As has been demonstrated recently, reaction (5) can lead to cage opening and subsequent 1,2 H-shift, thereby producing three structural isomers of Ama^+, including the canonical cage structure (Ama^+(**I**)), and two bicyclic distonic iminium ions (Ama^+(**II**) and Ama^+(**III**)), with primary and tertiary radical centers.[47] While Ama^+(**I**) will preferentially hydrogenate at the NH_2 group in reaction (6) leading to an ammonium cation, Ama^+(**II**) and Ama^+(**III**) will hydrogenate at the radical centers and thus form iminium cations.[67] Although reaction (6) is endothermic (by 74 kJ mol^{-1} for isomer **III** at the B3LYP-D3/cc-pVTZ level), there may be enough energy available in form of internal energy left in Ama^+ from reaction (5).

Collision-induced dissociation (CID) experiments are performed to confirm the chemical composition of the produced $AmaH^+Ar$ clusters (Fig. S2, ESI†). The generated $AmaH^+Ar$ clusters are mass-selected in the first quadrupole and irradiated in an adjacent octupole ion guide with a tuneable IR laser pulse (ν_{IR}) emitted from an optical parametric oscillator pumped by a nanosecond Q-switched Nd:YAG laser. The IR radiation is characterized by 10 Hz repetition rate, <4 cm^{-1} bandwidth, and pulse energies of 2–5 mJ and 0.1–0.5 mJ in the XH stretch (2600–3700 cm^{-1}) and fingerprint ranges (1100–1900 cm^{-1}). Frequency calibration to better than 1 cm^{-1} is performed using a wavemeter. Resonant vibrational excitation of the clusters leads exclusively to the loss of Ar. The $AmaH^+$ fragment ions are selected by the second quadrupole and monitored by a Daly detector as a function of the laser frequency to obtain the IRPD spectra of $AmaH^+Ar$. Separation of laser-induced dissociation from metastable decay background is achieved by triggering the ion source at twice the repetition rate of the laser and subtracting the signals from alternating triggers. All IRPD spectra are normalized for frequency-dependent variations in the photon flux.

Geometric, vibrational, energetic, and electronic properties of Ama, $AmaH^+$, and $AmaH^+Ar$ in their electronic ground states are characterized by quantum chemical calculations at the dispersion-corrected B3LYP-D3/cc-pVTZ level.[68] This computational

approach has already provided reliable results for Ama^+L_n clusters and is an efficient compromise between accuracy and computing time.[47,55,56] Relative energies and equilibrium binding energies (E_e, D_e) are corrected for harmonic zero-point vibrational energy to yield E_0 and D_0. To compensate for the different anharmonicity of the various CH/NH stretch and fingerprint modes, three different scaling factors are employed (0.9732, 0.9618, and 0.9491 for fingerprint and CH and NH stretch modes).[55] Computed IR stick spectra are convoluted with Gaussian line profiles (fwhm = 10 cm^{-1}) to facilitate convenient comparison with the measured IRPD spectra. Natural bond orbital (NBO) analysis is employed to evaluate the atomic charge distributions.[69,70] We only consider singlet electronic states, because triplets are computed to be very high in energy ($E_0 \geq 350$ kJ mol^{-1}). Cartesian coordinates and energies of all relevant structures are available in the ESI.†

3. Experimental results

Typical mass spectra of the EI source show the parent Ama^+ radical cation (m/z 151), its dehydrogenated and protonated closed-shell ions ($[Ama\text{-}H]^+/AmaH^+$ at m/z 150/152), and their clusters with Ar, N_2 and H_2O (Fig. S1, ESI†). Clusters with H_2O appear because traces of H_2O have been added to the gas inlet system for parallel experiments on $AmaH^+(H_2O)_n$ clusters. In addition, intense fragment ions of Ama^+ (F^+ at m/z 135, 108, 94, 57) are detected, consistent with the standard EI mass spectrum of Ama, confirming the identity of m/z 151 as Ama^+ (Fig. S1, ESI†).[54,71–73] Note that the standard EI mass spectrum of Ama is quite different from that of Ada, indicating the strong impact of the NH_2 group on the fragmentation process of the adamantyl cage.[54] One of the most intense peaks in the mass spectrum of the EI source (m/z 135) reveals the loss of NH_3 from $AmaH^+$,[58] most likely arising from fragmentation of N-protonated $AmaH^+$ into the very stable 1-adamantyl cation.[58] Further fragmentation of m/z 135 down to m/z 93 by elimination of C_3H_6 is only weakly observed,[58] possibly an indication for soft N-protonation of Ama. The CID spectrum of $AmaH^+Ar$ shows merely the loss of Ar, so that any significant isobaric mass contamination can be excluded (Fig. S2, ESI†).

The IRPD spectrum of $AmaH^+Ar$ recorded in the fingerprint (1100–1900 cm^{-1}) and XH stretch ranges (2700–3700 cm^{-1}) is shown in Fig. 1. The positions and widths of the transitions observed are listed in Table 1, along with the proposed vibrational and isomer assignments derived from the B3LYP-D3 calculations. The fingerprint range covers CH_2 torsion (τ_{CH_2}) and wagging (γ_{CH_2}) modes (**A–D**), and CH_2/NH_n bending (β_{CH_2/NH_n}) and CN stretching (ν_{CN}) fundamentals (**E–I**). The XH stretch range probes aliphatic CH_n stretch modes (ν_{CH_n}) of the Ama^+ moiety (**J–N**), overtone and combinations bands of $\beta_{NH_{2/3}}$ and ν_{CN} fundamentals (**O**, **P**, **T**), and symmetric and antisymmetric $\left(\nu^{s/a}_{NH_{2/3}}\right)$ NH stretch modes of the NH_2^+ (**S**, **U**) and NH_3^+ groups (**Q**, **R**).

To our initial surprise, we observe five bands in the NH stretch range (**Q–U**) and not just two, which one would expect for Ama protonated at the basic NH_2 group. The resulting

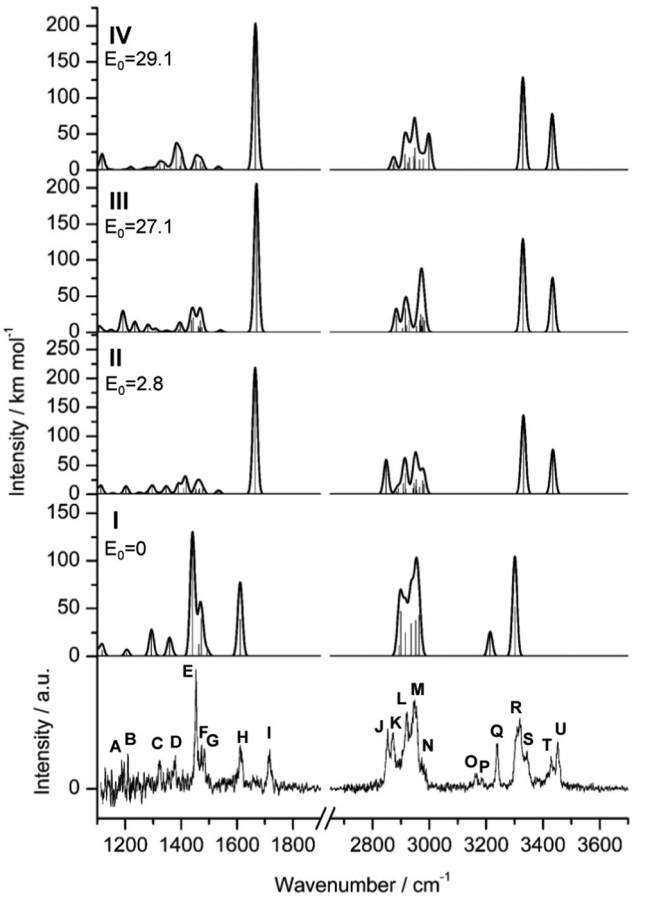

Fig. 1 IRPD spectra of $AmaH^+Ar$ in the XH stretch and fingerprint ranges compared to linear IR absorption spectra of Ama^+(**I–IV**) calculated at the B3LYP-D3/cc-pVTZ level (Tables S1 and S2, ESI†). The positions of the transitions observed (**A–U**) and their vibrational and isomer assignment are listed in Table 1. Relative energies (E_0) are given in kJ mol^{-1}.

ammonium ion of $AmaH^+$ with C_{3v} symmetry (RNH_3^+) has symmetric (a) and doubly degenerate antisymmetric (e) NH stretch modes, whereby the latter may split into two components upon Ar-tagging at the NH_3^+ group. By comparison with NH_4^+ and protonated aniline (AnH^+) and their complexes with rare gas atoms,[67,74] the ν_{NH_3} modes of the RNH_3^+ are expected in the 3150–3400 cm^{-1} range and may thus be associated with bands **Q**, **R**, and possibly **S**, observed at 3238, 3317, and 3344 cm^{-1}. On the other hand, ν_{NH_2} modes of amine cations (RNH_2^+), such as the NH_3^+, An^+, and the carbenium isomers of AnH^+,[67,75–77] have their NH stretch frequencies toward higher frequency (3350–3500 cm^{-1}), and such isomers of $AmaH^+$ may thus account for bands **U**, **T**, and possibly **S** observed at 3451, 3428, and 3344 cm^{-1}. Hence, the various intense NH stretch bands suggest the presence of at least two $AmaH^+$ isomers, one expected ammonium ion and one unexpected iminium ion. The larger width of **R** and its shoulder **S** may arise from effects of Ar-tagging, giving rise to a splitting upon symmetry reduction and minor shifts upon formation of NH···Ar hydrogen bonds (H-bonds). However, Ar-tagging of a single $AmaH^+$ isomer alone cannot account for the rich observed NH stretch spectrum with its large frequency spread.

Table 1 Positions, widths (fwhm in parenthesis) and vibrational and isomer assignments of the transitions observed in the IRPD spectrum of $AmaH^+Ar$ (Fig. 1)[a]

Peak	Mode	$AmaH^+Ar$	Isomer
A	τ_{CH_2}	1187 (12)	**I**, **II**[b]
B	τ_{CH_2}	1209 (2)	**I**, **II**[b]
C	γ_{CH_2}, τ_{CH_2}	1322 (8)	**I**, **II**[b]
D	γ_{CH_2}, τ_{CH_2}	1377 (11)	**I**, **II**[b]
E	$\gamma_{NH_3(umbrella)}$, β_{CH_2}	1453 (13)	**I**[b]
F	β_{CH_2}	1474 (6)	**I**, **II**[b]
G	β_{CH_2}, β_{CH_3}	1483 (5)	**I**, **II**[b]
H	β_{NH_3}	1611 (12)	**I**
I	β_{NH_2}	1714 (15)	**II**[b]
J	ν_{CH_n}	2853 (10)	**II**
K	ν_{CH_n}	2872 (7)	**II**[b]
L	ν_{CH_n}	2921 (14)	**I**, **II**[b]
M	ν_{CH_n}	2949 (17)	**I**, **II**[b]
N	ν_{CH_n}	2973 (5)	**II**[b]
O	$2\beta_{NH_3}$	3164 (7)	**I**
P	$2\beta_{NH_3}$	3185 (5)	**I**
Q	$\nu^s_{NH_3}$	3238 (13)	**I**
R	$\nu^a_{NH_3}$	3317 (21)	**I**
S	$\nu^s_{NH_2}$	3344 (7)	**II**[b]
T	$2\beta_{NH_2}$	3428 (11)	**II**[b]
U	$\nu^a_{NH_2}$	3451 (10)	**II**[b]

[a] All values are given in cm^{-1}. [b] Could be also assigned to the less stable isomers **III** and **IV**.

Similar to Ama^+Ar,[47] the aliphatic CH stretch range of $AmaH^+Ar$ (2800–3000 cm^{-1}) exhibits several bands (**J**–**N**), with two strong broader features **L** and **M** (2921 and 2949 cm^{-1}), one weak peak **N** in the blue shoulder of **M** (2973 cm^{-1}), and two low-frequency bands **J** and **K** with medium intensity (2853 and 2872 cm^{-1}). The two very weak bands **O** and **P** (3164 and 3185 cm^{-1}) between the CH and NH stretch ranges are probably overtones or combinations bands of $\beta_{NH_{2/3}}$ bend modes.

The fingerprint range is dominated by a very intense narrow band **E** at 1453 cm^{-1}, accompanied by two weaker sharp peaks **F** and **G** (1474 and 1483 cm^{-1}) in its blue shoulder. Interestingly, two broader and possibly unresolved features **H** and **I** at 1611 and 1714 cm^{-1} with comparable medium intensity occur in the $NH_{2/3}$ bending range, confirming the conclusion of the presence of (at least) two isomers drawn from the NH stretch range. Furthermore, one weak transition **A** (1187 cm^{-1}), one sharp peak **B** (1209 cm^{-1}), and two bands **C** and **D** with similar intensity (1322 and 1377 cm^{-1}) occur in the range of β_{CH_2}, γ_{CH_2}, τ_{CH_2}, and ρ_{NH_2}.

In addition to the $AmaH^+Ar$ dimer (n = 1), we have also recorded the IRPD spectra of $AmaH^+Ar_n$ with n = 2 and 3 in the XH stretch range. Similar to the case of Ama^+Ar_n,[48] the incremental spectral shifts and splittings upon tagging with further Ar ligands are very small and do not provide any additional information about the vibrational and isomer assignment. Hence, we do not discuss them in detail further here. The major information extracted from these IRPD spectra concerns the binding energy of the Ar ligands. The IRPD signal of $AmaH^+Ar_3$ is observed exclusively in the $AmaH^+$ monomer fragment channel, providing a rough upper limit of 1000 cm^{-1} for the Ar binding energy, fully consistent with the results of the B3LYP-D3 calculations detailed in Section 4.

4. Computational results and discussion

4.1. $AmaH^+$ isomers I–IV

Starting from neutral Ama and the previously detected Ama^+ radical cation isomers (Fig. S3, ESI†), stable structures of $AmaH^+$ are constructed by adding a proton to the basic NH_2 group of Ama or a H atom to the C radical centers of the open-cage Ama^+ isomers. Protonation of Ama at C is energetically highly unfavourable (when retaining the cage), because it would result in a fivefold coordinated C atom of the cycloalkane. The resulting $AmaH^+$ isomers **I**–**IV** are shown in Fig. 2, and their corresponding IR spectra are compared in Fig. 1 to the IRPD spectrum measured for $AmaH^+Ar$ (Table S1, ESI†). All relevant energies are listed in Table S2 (ESI†).

In the electronic ground state of neutral Ama ($^1A_1$, C_s), the NH_2 group is attached in a pyramidal configuration (sp^3 hybridisation of N) to the $C_{10}H_{15}$ cage *via* a C–N single bond (r_{CN} = 1.467 Å). The N–H bonds are relatively short (r_{NH} = 1.015 Å), leading to high-frequency symmetric and antisymmetric NH

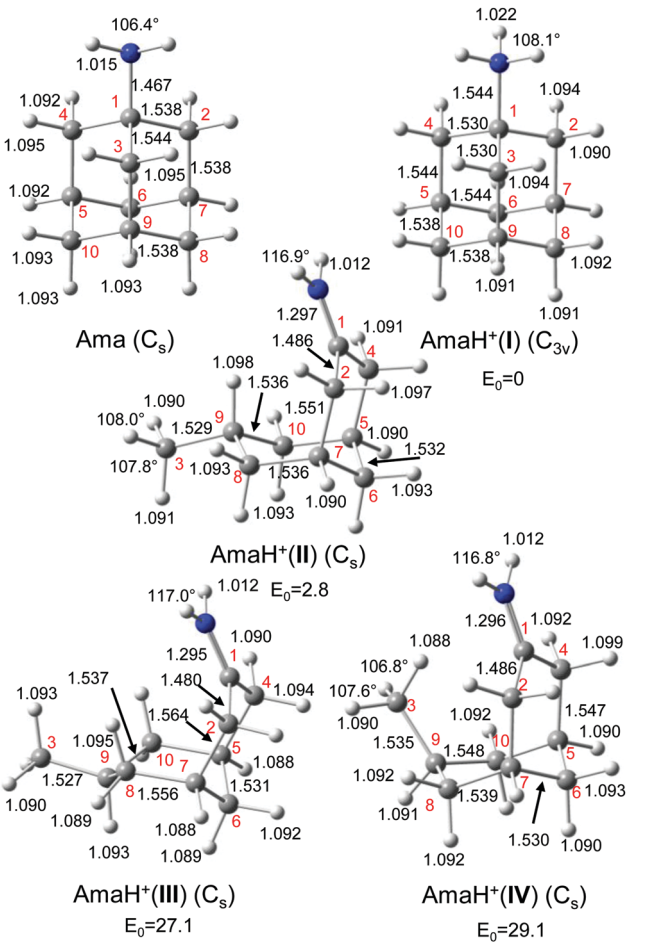

Fig. 2 Calculated equilibrium structures (in Å and degrees) of Ama and $AmaH^+$(**I**–**IV**) in their ground electronic state (B3LYP-D3/cc-pVTZ), along with numbering of the C atoms (in red). Relative energies (E_0) are given in kJ mol^{-1}.

stretch modes $\left(\nu^{s/a}_{NH_2} = 3285/3359\ cm^{-1}\right)$, with very low IR oscillator strength (3/0.2 km mol^{-1}). In general, the calculated structure and IR spectrum of Ama agree well with previous experimental and computational data.[51–54] Protonation of Ama at the NH_2 group produces the ammonium isomer **I** of AmaH$^+$ with C_{3v} symmetry in the $^1A_1$ electronic ground state, with a computed proton affinity (PA = 957 kJ mol^{-1}) in close agreement with the experimental value (PA = 949 kJ mol^{-1}).[78] This structure is indeed the global minimum on the AmaH$^+$ potential (E_0 = 0 kJ mol^{-1}). N-Protonation of Ama causes a drastic elongation of the N–H bonds by 7 mÅ to 1.022 Å and a slight increase in the NH_2 angle to 108.1°, while preserving the pyramidal configuration. The former effect results in massive ν_{NH} red shifts of ∼70/60 cm^{-1} ($\nu^{s}_{NH_{2/3}} = 3285$ *vs.* 3214 cm^{-1}, $\nu^{a}_{NH_{2/3}} = 3359$ *vs.* 3301 cm^{-1}, Fig. S4 and Table S3, ESI†). Moreover, the IR intensities of ν_{NH_3} are drastically enhanced (by a factor ∼10/500) due to the increased charge on the NH protons (q_H = 0.429 *e*) and thus can readily be detected by IRPD. However, the increase in IR activity is smaller than for Ama$^+$ (factor ∼100/350), for which the ν_{NH_2} modes are blue-shifted compared to Ama (Table S4, ESI†). Furthermore, the formation of the third N–H bond produces an additional intense γ_{NH_3} umbrella inversion mode at 1441 cm^{-1} ($I_{\gamma NH_3}$ = 130 km mol^{-1}), which is typical for NH_3^+ groups.[79] The degenerate β_{NH_3} modes (β_{NH_3} = 1611 cm^{-1}, $I_{\beta_{NH_3}}$ = 39 km mol^{-1}) have almost the same frequency and intensity as the β_{NH_2} mode of Ama (β_{NH_2} = 1609 cm^{-1}, $I_{\beta_{NH_2}}$ = 34 km mol^{-1}). In contrast to ionization of Ama, protonation lengthens the C–N single bond by 77 mÅ to 1.544 Å and shortens the adjacent C–C bonds (r_{C1C2} = 1.530 *vs.* 1.538 Å, r_{C1C3} = 1.530 *vs.* 1.544 Å), which is due to the higher positive charge on the NH_3^+ group (q_{NH_3} = 0.605 *e*) and its electron-withdrawing character. Moreover, the C–C bonds parallel to the C_3 symmetry axis are slightly elongated compared to Ama (r_{C4C5} = 1.544 *vs.* 1.538 Å). Almost all C–H bonds contract slightly (Δr_{CH} = 2 mÅ) resulting in blue shifts of the ν_{CH} bands (ν_{CH} = 2890 *vs.* 2899 cm^{-1}, ν_{CH} = 2917 *vs.* 2956 cm^{-1}). The highest occupied molecular orbital (HOMO) has CC σ character and extends over the whole adamantyl cage, while it has no amplitude at the NH_3^+ group (Fig. S5, ESI†).

The AmaH$^+$(**II**) isomer ($^1A'$, C_s, E_0 = 3.0 kJ mol^{-1}) is almost isoenergetic with the global minimum and formally derived from the open-cage Ama$^+$(**III**) radical cation isomer by adding a H atom at its tertiary C9 radical center. As shown recently, ionization of Ama can trigger a rearrangement reaction, producing *via* cage opening and subsequent 1,2 H-shift the bicyclic distonic Ama$^+$(**III**) iminium radical cation (involving a barrier of V_b = 123 kJ mol^{-1}), whose C9 radical center is a good acceptor for a H radical.[47,48] Consequently, AmaH$^+$(**II**) has also an open-cage structure with one CH_3 group ($C3H_3$) and a C9H group with its C–H bond oriented toward the nearly planar CNH_2^+ group ($r_{C9H\cdots C1}$ = 2.450 Å). As a result, the cage opens much more than for Ama$^+$(**III**) (θ_{C1C9C3} = 155.3° *vs.* 106.1°, $r_{C1\cdots C3}$ = 4.47 *vs.* 3.35 Å),[47] and the C–C bonds at the former C9 radical center drastically elongate (r_{C3C9} = 1.482 *vs.* 1.529 Å, r_{C9C8} = 1.492 *vs.* 1.536 Å). Moreover, the C2–C7/C4–C5 bonds are slightly stretched by 9 mÅ to 1.551 Å, whereas the remaining C–C bonds contract (r_{C1C2} = 1.491 *vs.* 1.486 Å, r_{C5C6} = 1.537 *vs.* 1.532 Å, r_{C7C8} = 1.543 *vs.* 1.536 Å). The cyclohexane ring carrying the NH_2^+ group has chair configuration as in Ama$^+$(**III**) and AmaH$^+$(**I**). The C–H bonds of the C atoms adjacent to C9 contract (Δr_{CH} = 4–8 mÅ), while most of the other C–H bonds elongate (Δr_{CH} = 1–2 mÅ). The newly formed C9–H bond is the longest bond (r_{CH} = 1.098 Å), which produces an intense ν_{CH} mode (ν_{CH} = 2848 cm^{-1}) significantly red-shifted from the other ν_{CH_n} modes. It may thus serve as indicator for this isomer. The N–H bonds of the planar CNH_2^+ group (sp^2 hybridization of N) of the iminium ion are stretched by 3 mÅ to 1.012 Å, while the NH_2 bond angle remains almost the same ($\Delta\theta_{NH_2}$ = 0.1°), resulting in a blue shift of $\nu^{s}_{NH_2}$ ($\nu^{s}_{NH_2} = 3331$ *vs.* 3358 cm^{-1}) and a slight red shift of $\nu^{a}_{NH_2}$ ($\nu^{a}_{NH_2} = 3435$ *vs.* 3433 cm^{-1}) compared to Ama$^+$(**III**).[47] However, the N–H bonds in AmaH$^+$(**II**) are much shorter than in AmaH$^+$(**I**), so that its NH_2 modes are well separated from the NH_3 modes ($\Delta\nu_{NH}$ ∼ 100 cm^{-1}). As with Ama$^+$(**III**),[47] a C=N double bond is present in AmaH$^+$(**II**), whose ν_{CN} mode couples with β_{NH_2}, resulting in a weak ν_{CN} band at 1534 cm^{-1} and an intense β_{NH_2} band at 1664 cm^{-1}. Compared to Ama$^+$(**III**), however, the C=N double bond is much shorter in AmaH$^+$(**II**), which leads to blue shifts in both β_{NH_2} and ν_{CN} by 34 and 23 cm^{-1}, respectively. Similar to Ama$^+$(**III**) (q_{CNH_2} = 0.608 *e*), most of the positive charge in AmaH$^+$(**II**) is located at the CNH_2^+ group (q_{CNH_2} = 0.748 *e*) and the HOMO is localized over the adamantyl framework (Fig. S5, ESI†).

The significantly less stable AmaH$^+$(**III**) iminium isomer ($^1A'$, C_s, E_0 = 27.4 kJ mol^{-1}) has a similar open-cage structure as AmaH$^+$(**II**), with one NH_2^+ and one CH_3 group but the C9–H bond pointing away from the CNH_2^+ group. The cage is less open than in AmaH$^+$(**II**) (θ_{C1C9C3} = 124.6° *vs.* 155.3°, $r_{C1\cdots C3}$ = 4.69 *vs.* 4.47 Å), and the second cyclohexane ring changes from chair to boat configuration. AmaH$^+$(**III**) can be formed by adding a H atom to either the primary C3 radical center of Ama$^+$(**II**) or the tertiary C9 radical center of Ama$^+$(**III**). The C2–C7/C4–C5 bonds and the C7–C8/C5–C10 bonds are elongated compared to AmaH$^+$(**II**) (r_{C2C7} = 1.564 *vs.*1.552 Å, r_{C7C8} = 1.556 *vs.* 1.536 Å), while the remaining C–C bonds differ only slightly (r_{C1C4} = 1.480 *vs.*1.486 Å, r_{C5C6} = 1.531 *vs.* 1.532 Å, r_{C8C9} = 1.537 *vs.* 1.537 Å, r_{C3C9} = 1.527 *vs.* 1.529 Å). Compared to AmaH$^+$(**II**), most C–H bonds contract only slightly (Δr_{CH} = 1–2 mÅ), while the C9–H bond contracts more (Δr_{C9H} = 5 mÅ), resulting in a blue shift of its ν_{CH} mode back to the other ν_{CH_n} bands (ν_{CH} = 2915 *vs.* 2848 cm^{-1}). The C=N double bond in AmaH$^+$(**III**) is slightly shorter than in AmaH$^+$(**II**) (r_{CN} = 1.295 *vs.* 1.297 Å), resulting in a small blue shift of the coupled β_{NH_2} and ν_{CN} modes by 8 and 6 cm^{-1}, respectively. The N–H bonds remain at r_{NH} = 1.012 Å with nearly unshifted $\nu^{s/a}_{NH_2}$ modes at 3329/3433 cm^{-1}. Similar to AmaH$^+$(**II**) (q_{CNH_2} = 0.748 *e*), most of the positive charge is located at the CNH_2^+ group (q_{CNH_2} = 0.755 *e*), and the HOMO is localized over the adamantyl framework (Fig. S5, ESI†).

The AmaH$^+$(**IV**) iminium isomer ($^1A'$, C_s, E_0 = 29.5 kJ mol^{-1}) has a similar structure (both differ only in conformation) as the slightly more stable AmaH$^+$(**III**) minimum and may formally be obtained by addition of an H radical to a radical site of Ama$^+$(**II**) or Ama$^+$(**III**). However, it is also possible that AmaH$^+$(**IV**) is formed by C3-protonation of Ama accompanied by cage opening.

The protonation energy for C3-protonation of Ama (927 kJ mol^{-1}) followed by cage opening is only slightly lower than the proton affinity for N-protonation of Ama (PA = 957 kJ mol^{-1}). The AmaH$^+$(**IV**) structure differs from **III** mainly by a more closed cage (θ_{C1C9C3} = 73.1° *vs.* 124.6°, $r_{C1\cdots C3}$ = 3.25 *vs.* 4.69 Å) and a chair configuration of the second cyclohexane ring. Consequently, most of the C–C bonds are stretched compared to AmaH$^+$(**III**) (r_{C1C4} = 1.486 *vs.*1.480 Å, r_{C8C9} =1.548 *vs.* 1.537 Å, r_{C3C9} = 1.535 *vs.* 1.527 Å), while the C–C bond lengths of the first amino-cyclohexane ring either decrease or remain the same (r_{C2C7} = 1.547 *vs.* 1.565 Å, r_{C7C8} = 1.539 *vs.* 1.556 Å, r_{C5C6} = 1.530 *vs.* 1.531 Å). The variation in the C–H bond lengths is increased from Δr_{CH} = 7 mÅ in AmaH$^+$(**III**) (1.088–1.095 Å) to Δr_{CH} = 11 mÅ in AmaH$^+$(**IV**) (1.088–1.099 Å), leading to four better resolved single convoluted bands (ν_{CH_n} = 2874, 2916, 2948, 2998 cm^{-1}). In particular, the shortened C3–H bond oriented toward the NH_2^+ group produces a blue shift in the ν_{CH_3} mode by $\Delta\nu_{CH_3}$ = 94 cm^{-1} to 2998 cm^{-1}. The C=N double bond is slightly elongated to r_{CN} = 1.296 Å, while the N–H bond lengths remain the same (r_{NH} = 1.012 Å). As a result, the coupled β_{NH_2} and ν_{CN} modes are slightly red-shifted to ν_{CN} = 1533 cm^{-1} and β_{NH_2} = 1665 cm^{-1}, while the ν_{NH_2} frequencies remain the same ($\nu^s_{NH_2}$ = 3329 cm^{-1}, $\nu^a_{NH_2}$ = 3432 cm^{-1}). Again, most of the positive charge is located at the CNH_2^+ group (q_{CNH_2} = 0.758 *e*) and the HOMO is localized over the adamantyl framework (Fig. S5, ESI†).

4.2 AmaH$^+$Ar clusters

Inspection of Fig. 1 reveals that the predictions for the three iminium isomers **II–IV** of AmaH$^+$ are rather similar, while that of the ammonium ion **I** is rather different, mainly due to the difference in N–H bonding and resulting IR spectra between the NH_3^+ and NH_2^+ groups. Prior to detailed comparison to experiment, we briefly consider the impact of Ar-tagging. The effect of Ar on the structural, vibrational, and energetic properties of all AmaH$^+$ isomers is indeed very small, so that the discussion on the AmaH$^+$Ar isomers is kept short. Details of the computed AmaH$^+$Ar structures, energies, charge distributions, and IR spectra are provided in the ESI† (Fig. S6–S10 and Tables S5, S6). In the most stable AmaH$^+$Ar isomers, Ar interacts with both the charged $NH_{2/3}^+$ group and the $C_{10}H_{15/16}$ moiety to maximize induction and dispersion forces, with low binding energies of D_0 = 10.2, 9.8, 6.9, and 8.9 kJ mol^{-1} for **I–IV**, respectively. Significantly, the minor differences in the Ar binding energy are too small to affect the energetic order of the monomer ions. The main impact of the weak interaction with Ar is a reduction in symmetry, resulting in a small splitting of the degenerate NH stretching and bending modes of AmaH$^+$(**I**). The IR spectra calculated for all AmaH$^+$Ar isomers for each monomer (**I–IV**) show only minimal shifts of less than 11 (**I**), 4 (**II**), 7 (**III**), and 8 cm^{-1} (**IV**) in $\nu_{NH_{2/3}}$, $\beta_{NH_{2/3}}$, γ_{NH_3}, and ν_{CN} upon Ar-tagging, respectively. Similar to Ama$^+$Ar,[47,48] the Ar ligands form in the most stable AmaH$^+$Ar isomers weak and strongly nonlinear NH$\cdots$Ar H-bonds ($R_{NH\cdots Ar}$ = 2.58–2.86 Å, ϕ_{ArHN} = 119.8–165.4°), accompanied by additional van der Waals contacts to adjacent CH_2/CH_3 groups ($R_{CH\cdots Ar}$ = 2.96–3.15 Å), yielding D_0 = 8.7–10.3 kJ mol^{-1}. As a result, the involved N–H bonds are slightly stretched (by 1 mÅ), while the involved C–H bonds are shortened (by 1 mÅ) and free C–H bonds can be elongated. These structural effects result in minor red and blue shifts in $\nu_{NH_{2/3}}$ (<11 cm^{-1}), ν_{CH_2} (<6 cm^{-1}) and ν_{CH_3} modes (<13 cm^{-1}). Charge transfer from AmaH$^+$ to Ar is rather small (5–9 m*e*). AmaH$^+$(**I**)–Ar(**I**) with the ammonium core ion has the strongest and a nearly linear NH$\cdots$Ar H-bond ($R_{NH\cdots Ar}$ = 2.58 Å, ϕ_{ArHN} = 165.4°), with the largest accompanying charge transfer of 9 m*e*. Due to Ar attachment, the two degenerate $\nu^a_{NH_3}$ (3301 cm^{-1}) and $\beta^a_{NH_3}$ (1611 cm^{-1}) modes of AmaH$^+$(**I**) split into two separate modes in AmaH$^+$(**I**)–Ar(**I**), $\nu^a_{NH_3}$ = 3289/3303 cm^{-1} and $\beta^a_{NH_3}$ = 1611/1613 cm^{-1}. In AmaH$^+$(**II**)–Ar(**I**), Ar binds to the NH_2^+ and C9H groups, resulting in a blue shift of the corresponding ν_{CH} mode from 2847 to 2860 cm^{-1}. In the less stable **I**-Ar(**II–V**), **II**-Ar(**II–VI**), **III**-Ar(**II–VI**), and **IV**-Ar(**II–VI**) clusters, Ar binds only to the $C_{10}H_{15/16}$ cage, with lower binding energies of D_0 = 2.0–6.2 kJ mol^{-1} and negligible effects on the monomer properties.

4.3 Assignment of IRPD spectrum

The minor effects of Ar-tagging on the geometries, energies, and IR spectra of the AmaH$^+$ isomers **I–IV** justify direct comparison of the latter to the measured IRPD spectrum of AmaH$^+$Ar for vibrational and isomer assignments (Table S1, ESI†). Inspection of Fig. 1 reveals immediately the presence of both ammonium and iminium isomers of AmaH$^+$. As outlined above, the NH stretch and bend ranges are most decisive. While most of the intense features are readily assigned to the most stable ammonium ion **I**, with clear signatures of the NH_3^+ group (**E**, **H**, **Q**, **R**), the strong features **I**, **S**, **T**, and **U** cannot be explained by this isomer but fit well to the features of the NH_2^+ group of the iminium isomers **II-IV**. Specifically, peaks **Q** and **R** (3238 and 3317 cm^{-1}) are attributed to the $\nu^s_{NH_3}$ and degenerate $\nu^a_{NH_3}$ NH stretch modes predicted at 3214 and 3301 cm^{-1} of **I**, respectively, while bands **E** and **H** (1453 and 1611 cm^{-1}) arise from the γ_{NH_3} umbrella (1441 cm^{-1}) and degenerate β_{NH_3} bending modes (1611 cm^{-1}), with maximum, mean, and median deviations of 24, 13, and 14 cm^{-1}, respectively, consistent with the widths of the bands (12–21 cm^{-1}) and the small effect of Ar-tagging ($\leq$5 cm^{-1}). Actually, bands **H** and **R** assigned to the doubly degenerate modes are broader than bands **E** and **Q** attributed to single transitions, which can readily be explained by splittings of the degenerate modes upon Ar-tagging into two unresolved components with roughly equal intensity. While the predicted splitting for β_{NH_3} is rather small (2 cm^{-1}), that for $\nu^a_{NH_3}$ is larger (13 cm^{-1}) and indeed partly resolved for band **R** (10 cm^{-1}).

Unfortunately, the properties of the NH_2^+ groups and resulting IR spectra of the iminium ions **II–IV** are very similar, with differences of $\leq$2/3 and $\leq$5 cm^{-1} for $\nu^{s/a}_{NH_2}$ and β_{NH_2}, respectively. Hence, we cannot distinguish between them at the current spectral resolution and consider for the assignment given here the by far most stable of them (**II**). Following this scenario, bands **S** and **U** (3344 and 3451 cm^{-1}) are assigned to $\nu^s_{NH_2}$ (3331 cm^{-1})

and $\nu^{a}_{NH_2}$ (3435 cm^{-1}) of **II**, with deviations of 13 and 16 cm^{-1}, respectively. Peak **I** (1714 cm^{-1}) is then attributed to β_{NH_2} (1664 cm^{-1}) of **II** which couples strongly with ν_{CN}. The somewhat larger deviation of 50 cm^{-1} between experiment and calculation is probably due to the different anharmonicity of the ν_{CN} mode, leading to an improper description of the coupling (including a nonoptimal scaling factor).[47] Due to its low intensity, ν_{CN} of **II** is not observed. Band **T** (3428 cm^{-1}) occurs also in the NH stretch range of the NH_2 group and may be attributed to a $\nu^{a}_{NH_2}$ mode of, for example, **III** or **IV**. This option implies that the large splitting between **T** and **U** of 23 cm^{-1} is not reproduced by the calculations for **II–IV**. An assignment of **T** and **U** to different Ar binding sites of **II** appears also unlikely, because the predicted shifts upon tagging are less than 4 cm^{-1}. A third alternative is an assignment of **T** to the $2\beta_{NH_2}$ overtone, which gains intensity *via* a classical Fermi resonance with ν_{NH_2}. Such intense $2\beta_{NH_2}$ overtones are also observed in the IRPD spectra of Ama^+L_n clusters, and indeed the position of band **T** is twice the frequency of band **I** (1714 cm^{-1}), making this interpretation a likely and currently favored scenario.

The assignments of the NH stretch and bend ranges reveal the presence of both ammonium and iminium ions. Their population ratio can roughly be estimated from the observed integrated peak intensities, the computed IR cross sections, and the reasonable assumptions of similar Ar-tagging and photodissociation efficiencies. When considering the isolated peaks **H** and **I**, or peaks **Q** and **U**, population ratios of 4 : 1 and 3 : 1 are obtained for **I** and **II**(–**IV**), *i.e.*, the $AmaH^+$ population and $AmaH^+Ar$ spectrum is strongly dominated by the ammonium isomer obtained by simple protonation of Ama at the NH_2 group.

With this derived population ratio, we consider now the other spectral ranges, for which clear-cut isomer assignments are less obvious due to similar frequencies and/or spectral congestion. Bands **B–D** (1209, 1322, 1377 cm^{-1}) are consistent with τ_{CH_2} and γ_{CH_2} modes of the dominant isomer **I** with respect to both frequency (1206, 1294, 1359 cm^{-1}) and relative intensity. Similarly, peaks **F** and **G** (1474 and 1483 cm^{-1}) can be attributed to β_{CH_n} modes of **I** (1469 cm^{-1}), with its strongest IR active modes at 1463 and 1472 cm^{-1} (26 and 39 km mol^{-1}). The transitions predicted for the minor isomer **II** in this spectral range mostly overlap (Table S1, ESI†), and the only isomer-specific transition appears to be band **A** (1187 cm^{-1}), which has no predicted mode of **I** but fits to τ_{CH_2} of **II** (1203 cm^{-1}).

In the CH stretch range, isomer-specific assignments are not as straightforward due to the similar frequencies of ν_{CH_n} of **I** and **II**, but bands **K** (2872 cm^{-1}) and **M** (2949 cm^{-1}) may be assigned to **I** (ν_{CH_n} = 2899 and 2956 cm^{-1}) and bands **J** (2853 cm^{-1}), **L** (2921 cm^{-1}), and **N** (2973 cm^{-1}) to **II** (ν_{CH_n} = 2848, 2917, and 2977 cm^{-1}) with maximum, mean, and median deviations of 27, 9, and 5 cm^{-1}. In particular, peak **J** (2853 cm^{-1}) agrees well with the blue-shifted ν_{CH} mode of **II** (2847 cm^{-1}), which is another argument for observing **II**, because none of the other isomers have modes predicted in this frequency range.

The weak bands **O** and **P** (3164 and 3185 cm^{-1}) cannot readily be explained by fundamentals of **I–IV** and thus are likely overtones and combination bands of β_{NH_2} and/or ν_{CN}. Similar bands have been observed previously for Ama^+Ar (3151 cm^{-1}) and AnH^+Ar (3175 cm^{-1}).[47,67] In analogy to assigning **T** as overtone of **H** of isomer **II**, **O** and **P** are attributed to overtones of the two components of **H** (1611 cm^{-1}). In this scenario, the splitting of the degenerate fundamental upon Ar-tagging is better resolved for the overtone. The corresponding expected overtone of **E** falls in the rich ν_{CH} range (2906 cm^{-1}) and is not easily identified.

4.4 Potential energy diagram and production routes

The analysis of the IRPD spectrum of $AmaH^+Ar$ by B3LYP-D3 calculations reveals the unambiguous spectroscopic fingerprints of (at least) two different $AmaH^+$ isomers in the supersonic plasma expansion: the dominant ammonium isomer (**I**) and the minor iminium isomer (**II**). The similar iminium ions **III** and **IV** cannot be completely ruled out because they have similar predicted IR spectra as **II**. However, due to their higher relative energy ($E_0 \geq 27$ kJ mol^{-1}), their formation is considered unlikely (although kinetic trapping may lead to their significant population). Assuming that only **I** and **II** are observed, their population ratio is derived in the range 3 : 1 to 4 : 1.

In an effort to rationalize possible production routes for **I** and **II**, we consider the potential energy diagram for Ama, and the various Ama^+ and $AmaH^+$ isomers in Fig. 3. The ionization process of Ama and the formation of the three isomers **I–III** of Ama^+ by vertical ionization and structural rearrangement reactions (cage opening and 1,2, H-shift) have been discussed in detail previously (Fig. S3, ESI†).[47] In a bare Ar expansion of Ama, the population ratio of **I–III** was determined as 10 : 3 : 7, although this may change somewhat in a H_2/Ar/He plasma employed here. Starting from Ama, two main reaction pathways are possible. The first route involves N-protonation of Ama most likely by exothermic proton transfer from H_3^+ (eqn (3)). The second route involves EI/CI of Ama, and subsequent H-addition to isomers **I–III** of Ama^+, most likely by H-abstraction from H_2 (eqn (5) and (6)), although internal energy resulting from EI/CI is required to overcome the endothermicity of this reaction. The ammonium ion **I** of $AmaH^+$ can be produced by either route, namely N-protonation of Ama or H_2 reacting with Ama^+(**I**). On the other hand, the iminium ions **II–IV** of $AmaH^+$ are most likely formed *via* the second route, involving EI/CI of Ama and H_2 reacting with Ama^+(**II**,**III**). However, C-protonation of Ama followed by cage opening, which would lead to $AmaH^+$(**IV**), cannot be completely ruled out, because of the comparable protonation energy of 927 kJ mol^{-1}. Moreover, protonation of Ama with H_3^+ leading to $AmaH^+$(**I**) is highly exothermic and thus may also produce **II–IV** by cage opening.

In $AmaH^+$(**I**), N-protonation at the N lone pair elongates the C–N bond and contracts the adjacent C1–C3 bonds, thereby preventing cage opening with an intact NH_3^+ group. The calculated proton affinity for N-protonation is in good agreement with experiment (PA = 957 *vs.* 949 kJ mol^{-1}).[78] Starting from the $AmaH^+$(**I**) global minimum, a 1,2 H-shift from the NH_3^+ group to the $C3H_2$ group can occur, which opens the cage and forms $AmaH^+$(**IV**) at E_0 = 29.5 kJ mol^{-1}. However, the

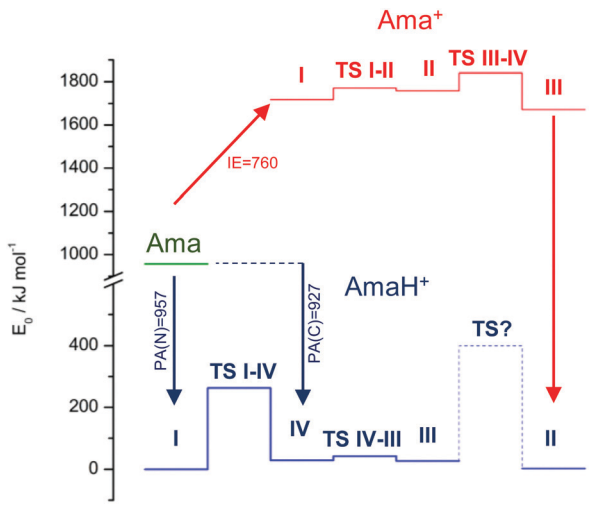

Fig. 3 Potential energy surfaces (minima and transition states) of $AmaH^+$ (blue), Ama^+ (red), and Ama (green) for the protonation and ionization pathways including cage-opening processes. Ionization energy (IE) and proton affinity (PA) values are given in kJ mol^{-1}.

energy barrier for this rearrangement process at TS(**I–IV**) is rather high (V_b = 263 kJ mol^{-1}), making this process unlikely. Nonetheless, from $AmaH^+$(**IV**) the cage can open further *via* TS(**IV–III**) at a very low barrier (V_b = 14 kJ mol^{-1}) to form $AmaH^+$(**III**) at E_0 = 27.4 kJ mol^{-1} (**III** and **IV** differ only in their conformation). This rearrangement is accompanied by a chair to boat conversion of the cyclohexane ring. A rearrangement from $AmaH^+$(**III**) to $AmaH^+$(**II**) is rather improbable, since this process would require most of the structure ($C_6H_8NH_2$) to flip once around the C8–C10 axis, which probably involves a high barrier. Because of this substantial rearrangement, the associated barrier for TS(**III–II**) could not be calculated. Hence, we assume that the detected $AmaH^+$(**II**) isomer cannot be formed via the protonation pathway and therefore must be formed via the ionization route.

Unlike N-protonation of Ama, ionization leads to a contraction of the C–N bond and a drastic elongation of the C1–C3 bond in Ama^+(**I**) (E_0 = 45.9 kJ mol^{-1}) due to the removal of an electron from the N lone pair and the increased delocalization of this orbital into the adamantyl cage. The computed adiabatic ionization energy of 7.9 eV agrees well with the estimated vertical value (8.6 eV),[53] and both are well below the available maximum electron energy of the EI process (220 eV). As a result, part of the nascent Ama^+(**I**) population may overcome the energy barrier at **TS(I–II)** (V_b = 54.1 kJ mol^{-1}, E_0 = 100.0 kJ mol^{-1}) for opening the cage. This process generates the bicylic distonic Ama^+(**II**) iminium ion (E_0 = 87.4 kJ mol^{-1}) with a primary $CH_2^\bullet$ radical center. A much more stable tertiary $CR_3^\bullet$ radical center is then formed in the most stable distonic bicyclic iminium ion Ama^+(**III**) (E_0 = 0) by 1,2 H-shift from C9H to $CH_2^\bullet$ *via* Ama^+(**TS(II–III)**) (V_b = 81.6 kJ mol^{-1}). This tertiary $CR_3^\bullet$ radical center is the very attractive for H-atom attachment leading to the formation of $AmaH^+$(**II**). As Ama^+(**III**) has already been detected in high abundance in the Ar plasma expansion of Ama,[47] this formation mechanism of the low-energy $AmaH^+$(**II**) isomer (E_0 = 3.0 kJ mol^{-1}) is highly plausible.

6. Concluding remarks

In conclusion, we characterize herein the structural, vibrational, and energetic properties of $AmaH^+$ ions by Ar-tagging IRPD spectroscopy and dispersion-corrected B3LYP-D3 calculations. To this end, the $AmaH^+$ ions are generated in a supersonic plasma expansion generated by electron/chemical ionization of a molecular beam containing Ama, He, and Ar. Significantly, the obtained IRPD spectrum of $AmaH^+Ar$ provides the first spectroscopic characterization of the structure of this pharmaceutically active ion. The influence of Ar is shown to be negligible by B3LYP-D3 calculations and the evolution of IRPD spectra recorded for $AmaH^+Ar_n$ with n = 1–3. The IRPD spectra cover the structure-sensitive NH stretch and bend ranges, which reveal the presence of two types of isomers. The dominant population corresponds to N-protonated $AmaH^+$, which is the global minimum on the computed potential energy surface (isomer **I**, E_0 = 0) and the relevant structure for pharmaceutical applications in solution. In addition to this ammonium ion, a smaller population is assigned to the only slightly less stable bicyclic iminium ion (isomer **II**, E_0 = 3 kJ mol^{-1}), which is probably produced by ionization of Ama, followed by opening of the adamantyl cage and subsequent addition of H. A study on $AmaH^+(H_2O)_n$ clusters using similar experimental and computational techniques is underway to characterize the impact of microhydration on the structure and reactivity of this fundamental biomolecular ion.

Conflicts of interest

There are no conflicts of interest to declare.

Acknowledgements

This study was supported by Deutsche Forschungsgemeinschaft (grant DO 729/8). We thank P. R. Schreiner for valuable discussions about the structure and reactivity of diamondoid cations.

References

1 S. Landa and V. Machacek, Adamantane, a new hydrocarbon extracted from petroleum, *Collect. Czech. Chem. Commun.*, 1933, **5**, 1.
2 J. E. Dahl, S. G. Liu and R. M. K. Carlson, Isolation and structure of higher diamondoids, nanometer-sized diamond molecules, *Science*, 2003, **299**, 96–99.
3 R. Schleyer and P. von, A simple preparation of adamantane, *J. Am. Chem. Soc.*, 1957, **79**, 3292.
4 R. C. Fort and P. v R. Schleyer, Adamantane: Consequences of the diamondoid structure, *Chem. Rev.*, 1964, **64**, 277–300.
5 J. E. P. Dahl, J. M. Moldowan, Z. Wei, P. A. Lipton, P. Denisevich, R. Gat, S. Liu, P. R. Schreiner and R. M. K. Carlson, Synthesis of higher diamondoids and implications for their formation in petroleum, *Angew. Chem., Int. Ed.*, 2010, **49**, 9881–9885.

6 P. R. Schreiner, L. V. Chernish, P. A. Gunchenko, E. Y. Tikhonchuk, H. Hausmann, M. Serafin, S. Schlecht, J. E. P. Dahl, R. M. K. Carlson and A. A. Fokin, Overcoming lability of extremely long alkane carbon–carbon bonds through dispersion forces, *Nature*, 2011, **477**, 308.
7 W. L. Yang, J. D. Fabbri, T. M. Willey, J. R. I. Lee, J. E. Dahl, R. M. K. Carlson, P. R. Schreiner, A. A. Fokin, B. A. Tkachenko and N. A. Fokina, Monochromatic electron photoemission from diamondoid monolayers, *Science*, 2007, **316**, 1460–1462.
8 D. F. Blake, F. Freund, K. F. M. Krishnan, C. J. Echer, R. Shipp, T. E. Bunch, A. G. Tielens, R. J. Lipari, C. J. D. Hetherington and S. Chang, The nature and origin of interstellar diamond, *Nature*, 1988, **332**, 611.
9 R. S. Lewis, E. Anders and B. T. Draine, Properties, detectability and origin of interstellar diamonds in meteorites, *Nature*, 1989, **339**, 117.
10 J.-Y. Raty and G. Galli, Ultradispersity of diamond at the nanoscale, *Nat. Mater.*, 2003, **2**, 792.
11 P. R. Schreiner, N. A. Fokina, B. A. Tkachenko, H. Hausmann, M. Serafin, J. E. P. Dahl, S. Liu, R. M. K. Carlson and A. A. Fokin, Functionalized nanodiamonds: Triamantane and [121] tetramantane, *J. Org. Chem.*, 2006, **71**, 6709–6720.
12 K. Gerzon, E. V. Krumkalns, R. L. Brindle, F. J. Marshall and M. A. Root, The adamantyl group in medicinal agents. I. Hypoglycemic *N*-arylsulfonyl-*N*′-adamantylureas, *J. Med. Chem.*, 1963, **6**, 760–763.
13 H. Schwertfeger, A. A. Fokin and P. R. Schreiner, Diamonds are a chemist's best friend: diamondoid chemistry beyond adamantane, *Angew. Chem., Int. Ed.*, 2008, **47**, 1022–1036.
14 A. A. Fokin and P. R. Schreiner, Selective alkane transformations *via* radicals and radical cations: Insights into the activation step from experiment and theory, *Chem. Rev.*, 2002, **102**, 1551–1594.
15 L. Wanka, K. Iqbal and P. R. Schreiner, The lipophilic bullet hits the targets: Medicinal chemistry of adamantane derivatives, *Chem. Rev.*, 2013, **113**, 3516–3604.
16 O. Pirali, M. Vervloet, J. E. Dahl, R. M. K. Carlson, A. Tielens and J. Oomens, Infrared spectroscopy of diamondoid molecules: New insights into the presence of nanodiamonds in the interstellar medium, *Astrophys. J.*, 2007, **661**, 919.
17 L. Landt, K. Klünder, J. E. Dahl, R. M. K. Carlson, T. Möller and C. Bostedt, Optical response of diamond nanocrystals as a function of particle size, shape, and symmetry, *Phys. Rev. Lett.*, 2009, **103**, 47402.
18 A. A. Fokin, P. R. Schreiner, P. A. Gunchenko, S. A. Peleshanko, T. y E. Shubina, S. D. Isaev, P. V. Tarasenko, N. I. Kulik, H.-M. Schiebel and A. G. Yurchenko, Oxidative single-electron transfer activation of σ-bonds in aliphatic halogenation reactions, *J. Am. Chem. Soc.*, 2000, **122**, 7317–7326.
19 M. Mella, M. Freccero, T. Soldi, E. Fasani and A. Albini, Oxidative functionalization of adamantane and some of its derivatives in solution, *J. Org. Chem.*, 1996, **61**, 1413–1422.
20 A. A. Fokin, B. A. Tkachenko, P. A. Gunchenko, D. V. Gusev and P. R. Schreiner, Functionalized nanodiamonds part I. An experimental assessment of diamantane and computational predictions for higher diamondoids, *Chem. – Eur. J.*, 2005, **11**, 7091–7101.
21 P. A. Gunchenko, A. A. Novikovskii, M. V. Byk and A. A. Fokin, Structure and transformations of diamantane radical cation: Theory and experiment, *Russ. J. Org. Chem.*, 2014, **50**, 1749–1754.
22 B. A. McGuire, 2018 census of interstellar, circumstellar, extragalactic, protoplanetary disk, and exoplanetary molecules, *Astrophys. J., Suppl. Ser.*, 2018, **239**, 17.
23 J. Cernicharo, B. Tercero, A. Fuente, J. L. Domenech, M. Cueto, E. Carrasco, V. J. Herrero, I. Tanarro, N. Marcelino and E. Roueff, Detection of the ammonium ion in space, *Astrophys. J., Lett.*, 2013, **771**, L10.
24 E. E. Etim, P. Gorai, A. Das and E. Arunan, Interstellar protonated molecular species, *Adv. Space Res.*, 2017, **60**, 709–721.
25 T. Henning and F. Salama, Carbon in the Universe, *Science*, 1998, **282**, 2204–2210.
26 P. B. Crandall, D. Müller, J. Leroux, M. Förstel and O. Dopfer, Optical spectrum of the adamantane radical cation, *Astrophys. J.*, 2020, **900**, L20.
27 W. L. Davies, R. R. Grunert, R. F. Haff, J. W. McGahen, E. M. Neumayer, M. Paulshock, J. C. Watts, T. R. Wood, E. C. Hermann and C. E. Hoffmann, Antiviral activity of 1-adamantanamine (amantadine), *Science*, 1964, **144**, 862–863.
28 R. S. Schwab, A. C. England, D. C. Poskanzer and R. R. Young, Amantadine in the treatment of Parkinson's disease, *JAMA*, 1969, **208**, 1168–1170.
29 G. Hubsher, M. Haider and M. S. Okun, Amantadine: The journey from fighting flu to treating Parkinson disease, *Neurology*, 2012, **78**, 1096–1099.
30 K. Spilovska, F. Zemek, J. Korabecny, E. Nepovimova, O. Soukup, M. Windisch and K. Kuca, Adamantane – A lead structure for drugs in clinical practice, *Curr. Med. Chem.*, 2016, **23**, 3245–3266.
31 J. W. Johnson and S. E. Kotermanski, Mechanism of action of memantine, *Curr. Opin. Pharmacol.*, 2006, **6**, 61–67.
32 C. G. Parsons, A. Stöffler and W. Danysz, Memantine: A NMDA receptor antagonist that improves memory by restoration of homeostasis in the glutamatergic system–too little activation is bad, too much is even worse, *Neuropharmacology*, 2007, **53**, 699–723.
33 J. S. Oxford and A. Galbraith, Antiviral activity of amantadine: A review of laboratory and clinical data, *Pharmacol. Ther.*, 1980, **11**, 181–262.
34 J. Hu, R. Fu and T. A. Cross, The chemical and dynamical influence of the anti-viral drug amantadine on the M2 proton channel transmembrane domain, *Biophys. J.*, 2007, **93**, 276–283.
35 I. V. Chizhmakov, F. M. Geraghty, D. C. Ogden, A. Hayhurst, M. Antoniou and A. Hay, J. Selective proton permeability and pH regulation of the influenza virus M2 channel expressed in mouse erythroleukaemia cells, *J. Physiol.*, 1996, **494**, 329–336.
36 WHO, WHO | Summary of influenza antiviral susceptibility surveillance findings, 2010–2011, retrieved 2019.

37 A. S. Monto and N. H. Arden, Implications of viral resistance to amantadine in control of influenza A, *Clin. Infect. Dis.*, 1992, **15**, 362–367.
38 R. P. Grelak, R. Clark, J. M. Stump and V. G. Vernier, Amantadine-dopamine interaction: possible mode of action in Parkinsonism, *Science*, 1970, **169**, 203–204.
39 L.-O. Farnebo, K. Fuxe, M. Goldstein, B. Hamberger and U. Ungerstedt, Dopamine and noradrenaline releasing action of amantadine in the central and peripheral nervous system: a possible mode of action in Parkinson's disease, *Eur. J. Pharmacol.*, 1971, **16**, 27–38.
40 P. F. von Voigtlander and K. E. Moore, Dopamine: Release from the brain in vivo by amantadine, *Science*, 1971, **174**, 408–410.
41 J. Kornhuber, M. Weller, K. Schoppmeyer and P. Riederer, Amantadine and memantine are NMDA receptor antagonists with neuroprotective properties, *J. Neural Transm.*, 1994, **43**, 91–104.
42 A. A. Spasov, T. V. Khamidova, L. I. Bugaeva and I. S. Morozov, Adamantane derivatives: Pharmacological and toxicological properties, *Pharm. Chem. J.*, 2000, **34**, 1–7.
43 T. J. Murray, Amantadine therapy for fatigue in multiple sclerosis, *Can. J. Neurol. Sci.*, 1985, **12**, 251–254.
44 K. M. Kampman, J. R. Volpicelli, A. I. Alterman, J. Cornish and C. P. O'Brien, Amantadine in the treatment of cocaine-dependent patients with severe withdrawal symptoms, *Am. J. Psychiatry*, 2000, **157**, 2052–2054.
45 J. Kornhuber, W. Retz and P. Riederer, Slow accumulation of psychotropic substances in the human brain. Relationship to therapeutic latency of neuroleptic and antidepressant drugs?, *J. Neural Transm. Suppl*, 1995, **46**, 315–324.
46 F. Weber and G. Sedelmeier, Top 200 drugs by worldwide sales 2013, *Nachr. Chem.*, 2014, **62**, 997.
47 M. A. R. George and O. Dopfer, Infrared spectrum of the amantadine cation: Opening of the diamondoid cage upon ionization, *J. Phys. Chem. Lett.*, 2022, **13**, 449–454.
48 M. A. R. George and O. Dopfer, Opening of the diamondoid cage upon ionization probed by infrared spectra of the amantadine cation solvated by Ar, N_2, and H_2O, *Chem. – Eur. J.*, 2022, DOI: **10.1002/chem.202200577**.
49 J. C. Garcia, J. F. Justo, W. V. M. Machado and L. V. C. Assali, Structural, electronic, and vibrational properties of amino-adamantane and rimantadine isomers, *J. Phys. Chem. A*, 2010, **114**, 11977–11983.
50 L. Rivas, S. Sanchez-Cortes, J. Stanicova, J. V. Garcia-Ramos and P. Miskovsky, FT-Raman, FTIR and surface-enhanced Raman spectroscopy of the antiviral and antiparkinsonian drug amantadine, *Vib. Spectrosc.*, 1999, **20**, 179–188.
51 C. Parlak and Ö. Alver, A density functional theory investigation on amantadine drug interaction with pristine and B, Al, Si, Ga, Ge doped C_{60} fullerenes, *Chem. Phys. Lett.*, 2017, **678**, 85–90.
52 P. C. Yates, T. J. Hill and M. Kaur, A molecular modelling study of the anti-viral agent amantadine and its derivatives, *THEOCHEM*, 1992, **258**, 299–313.
53 I. V. Litvinyuk, Y. Zheng and C. E. Brion, Electron momentum spectroscopy study of amantadine: Binding energy spectra and valence orbital electron density distributions, *Chem. Phys.*, 2000, **261**, 289–300.
54 P. J. Linstrom and W. G. Mallard, *NIST Chemistry WebBook, National Institute of Standards and Technology*, NIST Standards and Technology, Gaithersburg, MD, **https://webbook.nist.gov** (accessed 2022-02-01).
55 M. A. R. George, F. Buttenberg, M. Förstel and O. Dopfer, Microhydration of substituted diamondoid radical cations of biological relevance: infrared spectra of amantadine$^+$-$(H_2O)_{n=1-3}$ clusters, *Phys. Chem. Chem. Phys.*, 2020, **22**, 28123–28139.
56 M. A. R. George, M. Förstel and O. Dopfer, Infrared spectrum of the adamantane$^+$-water cation: Hydration-induced C–H bond activation and free internal water rotation, *Angew. Chem., Int. Ed.*, 2020, 12098–12104.
57 A. Patzer, M. Schütz, T. Möller and O. Dopfer, Infrared spectrum and structure of the adamantane cation: Direct evidence for Jahn–Teller distortion, *Angew. Chem., Int. Ed.*, 2012, **51**, 4925–4929.
58 M. Štícha, R. L. Chayrov and I. G. Stankova, Understanding the fragmentation pathways of carbocyclic derivatives of amino acids by using electrospray ionization tandem mass spectrometry, *Anal. Lett.*, 2019, **52**, 2069–2076.
59 J. W. Turczan and T. Medwick, NMR analysis of pharmaceuticals XII: Determination of amantadine hydrochloride in soft gelatin capsules and syrups, *J. Pharm. Sci.*, 1974, **63**, 425–427.
60 H. A. Omara and A. S. Amin, Spectrophotometric microdetermination of anti-Parkinsonian and antiviral drug amantadine HCl in pure and in dosage forms, *Arab. J. Chem*, 2011, **4**, 287–292.
61 A. M. Mahmoud, N. Y. Khalil, I. A. Darwish and T. Aboul-Fadl, Selective spectrophotometric and spectrofluorometric methods for the determination of amantadine hydrochloride in capsules and plasma *via* derivatization with 1,2-naphthoquinone-4-sulphonate, *Int. J. Anal. Chem.*, 2009, 810104.
62 Y. Dou, Y. Sun, Y. Ren, P. Ju and Y. Ren, Simultaneous non-destructive determination of two components of combined paracetamol and amantadine hydrochloride in tablets and powder by NIR spectroscopy and artificial neural networks, *J. Pharm. Biomed.*, 2005, **37**, 543–549.
63 O. Dopfer, IR spectroscopy of microsolvated aromatic cluster ions: Ionization-induced switch in aromatic molecule–solvent recognition, *Z. Phys. Chem.*, 2005, **219**, 125–168.
64 O. Dopfer, Spectroscopic and theoretical studies of CH_3^+-Rg_n clusters (Rg = He, Ne, Ar): From weak intermolecular forces to chemical reaction mechanisms, *Int. Rev. Phys. Chem.*, 2003, **22**, 437–495.
65 T. Oka, Interstellar H_3^+, *Proc. Natl. Acad. Sci. U. S. A.*, 2006, **103**, 12235–12242.
66 O. Dopfer, D. Roth, R. V. Olkhov and J. P. Maier, Infrared spectrum and *ab initio* calculations of the CH_3CNH^+-H_2 ionic complex, *J. Chem. Phys.*, 1999, **110**, 11911–11917.
67 F. M. Pasker, N. Solcà and O. Dopfer, Spectroscopic identification of carbenium and ammonium isomers of protonated

aniline (AnH^+): IR spectra of weakly bound AnH^+–L_n clusters (L = Ar, N_2), *J. Phys. Chem. A*, 2006, **110**, 12793–12804.

68 M. J. Frisch; *et al.*, *Gaussian 09, version D.01*, Gaussian, Inc., Wallingford, CT, 2009.

69 E. D. Glendening; J. K. Badenhoop; A. E. Reed; J. E. Carpenter; J. A. Bohmann; C. M. Morales; C. R. Landis and F. Weinhold, *NBO 6.0*, Theoretical Chemistry Institute, University of Wisconsin, Madison, 2013.

70 A. E. Reed, L. A. Curtiss and F. Weinhold, Intermolecular interactions from a natural bond orbital, donor–acceptor viewpoint, *Chem. Rev.*, 1988, **88**, 899–926.

71 R. J. Waltman and A. C. Ling, Mass spectrometry of diamantane and some adamantane derivatives, *Can. J. Chem.*, 1980, **58**, 2189–2195.

72 K. K. Khullar, C. L. Bell and L. Bauer, Mass spectrometry of 1-substituted adamantanes. Effect of functional groups on the primary fragmentation pathways, *J. Org. Chem.*, 1973, **38**, 1042–1044.

73 Z. Dolejšek, S. Hala, V. Hanuš and S. Landa, Adamantane and its derivatives. VIII. Mass spectra of derivatives of adamantane formed by substitution at C(1), *Collect. Czechoslov. Chem. Commun.*, 1966, **31**, 435–449.

74 O. Dopfer, S. A. Nizkorodov, M. Meuwly, E. J. Bieske and J. P. Maier, Microsolvation of the ammonium ion in argon: Infrared spectra of NH_4^+-Ar_n complexes (n = 1–7), *Int. J. Mass Spectrom.*, 1997, **167**, 637–647.

75 N. Solcà and O. Dopfer, Interaction between aromatic amine cations and quadrupolar ligands: Infrared spectra of aniline$^+$–$(N_2)_n$ (n = 1–5) complexes, *J. Phys. Chem. A*, 2002, **106**, 7261–7270.

76 O. Dopfer, Microsolvation of the ammonia cation in argon: I. *Ab initio* and density functional calculations of NH_3^+–Ar_n (n = 0–5), *Chem. Phys.*, 2002, **283**, 63–84.

77 O. Dopfer, N. Solcà, R. V. Olkhov and J. P. Maier, Microsolvation of the ammonia cation in argon: II. IR photodissociation spectra of NH_3^+–Ar_n (n = 1–6), *Chem. Phys.*, 2002, **283**, 85–110.

78 E. P. L. Hunter and S. G. Lias, Evaluated gas phase basicities and proton affinities of molecules: An update, *J. Phys. Chem. Ref. Data*, 1998, **27**, 413–656.

79 T. Khuu, N. Yang and M. A. Johnson, Vibrational spectroscopy of the cryogenically cooled O- and N-protomers of 4-aminobenzoic acid: Tag effects, isotopic labels, and identification of the *E*, *Z* isomer of the O-protomer, *Int. J. Mass Spectrom.*, 2020, **457**, 116427.